Remote Sensing of Environment 142 (2014) 103–110

Contents lists available at ScienceDirect

Remote Sensing of Environment

journal homepage: www.elsevier.com/locate/rse

A surface radiation climatology across two Meteosat satellite generations

R. Posselt [a,*], R. Mueller [b], J. Trentmann [b], R. Stockli [a], M.A. Liniger [a]

[a] Federal Office of Meteorology and Climatology MeteoSwiss, Zurich, Switzerland
[b] German Meteorological Service, Offenbach, Germany

ARTICLE INFO

Article history:
Received 13 May 2013
Received in revised form 18 October 2013
Accepted 12 November 2013
Available online 14 December 2013

Keywords:
Solar surface irradiance
Climate data records
Satellite remote sensing

ABSTRACT

Long-term observations of the surface radiation budget are essential for climate monitoring, climate model evaluation and solar energy applications. The Satellite Application Facility on Climate Monitoring (CM SAF) released a climate data record (CDR) of global and direct surface irradiance as well as effective cloud albedo derived from observations of the Meteosat First Generation satellites (MFG, 1983–2005). This study presents an extension of this CDR using measurements from the Meteosat Second Generation satellites (MSG, 2004–present). This extended surface radiation dataset spans nearly 30 years of data and, therefore, is in its uniquely high temporal and spatial resolution a valuable contribution to the climate community.

In order to enable climatological consistency and homogeneity, the retrieval algorithm had to be modified for MSG: 1. The two narrowband visible channels of the MSG satellites are combined to simulate the MFG broadband visible channel; 2. The maximum cloud reflectance is empirically adjusted to account for the differences in the dynamic range of MSG compared to MFG.

The extended dataset is tested for homogeneity and no significant breaks are detected during the overlap period of 2004–2005. Validation of the extended global radiation dataset against ground based observations from the Baseline Surface Radiation Network yields a mean monthly absolute bias of 8.15 W m^{-2}. This complies with the target accuracy threshold of 15 W m^{-2} defined by the Global Climate Observing System.

Global radiation has an overall positive, and significant, trend over the Meteosat disk which is mainly due to a negative trend in the effective cloud albedo, i.e., a decrease in cloudiness. Trends due to changes in the clear sky radiation are small and only induced by trends in the water vapor fields. Trends caused by changes in the direct effects of atmospheric aerosol are not represented because an aerosol climatology is used.

1. Introduction

Climate monitoring and analysis require the radiation budget at the earth's surface as a key parameter (GCOS, 2010; Solomon et al., 2007). It is of great importance for various applications such as agriculture, energy production and consumption, and infrastructure. With satellite data it is possible to retrieve the surface radiation budget at high spatial and temporal resolutions covering large areas (continental to global) (GCOS, 2006). The effect of the atmosphere and the earth's surface on the solar radiative fluxes is radiometrically measured by the satellite sensors. In particular, the strong negative correlation between solar radiation reflected back to space by clouds and the solar radiation reaching the earth's surface can be exploited by use of the so-called Heliosat method (Beyer, Costanzo, & Heinemann, 1996; Cano et al., 1986; Hammer et al., 2003).

The Satellite Application Facility for Climate Monitoring (CM SAF) has generated a climate data record (CDR) of solar surface radiation parameters (global radiation *SIS* and direct radiation *SID*) and effective cloud albedo *CAL* (Posselt, Mueller, Stöckli, & Trentmann, 2012; Posselt, Mueller, Stockli, & Trentmann, 2011) based on measurements in the visible range from the Meteosat First Generation Satellites which were operated from 1983 to 2005. CM SAF is part of the European Organization for the Exploitation of Meteorological Satellites (EUMETSAT) Satellite Application Facilities (SAFs). It develops and provides data records for climate monitoring derived from various satellites (Schulz et al., 2009).

The CM SAF surface radiation CDR is processed using the MagicSol algorithm. The cloud information is extracted from the satellite data using the Heliosat algorithm. The employed version was adapted for climate purposes by implementing a self-calibration method to account for satellite switches and sensor degradation and by introducing improved method for the retrieval of the clear-sky background image (Posselt et al., 2012). It employed the broadband visible channel (VISSN) of the MFG satellites. Further, MagicSol includes the Mesoscale Atmospheric Global Irradiance Code (MAGIC) for the calculation of the clear sky irradiances by the means of look-up-tables (Mueller, Matsoukas, Gratzki, Behr, & Hollmann, 2009).

Posselt, Mueller, Stöckli, and Trentmann (2011a) demonstrated that *CAL* depends on the instrument's spectral response function which

* Corresponding author.
E-mail address: rebekka.posselt@meteoswiss.ch (R. Posselt).

0034-4257
http://dx.doi.org/10.1016/j.rse.2013.11.007

becomes especially apparent over vegetated areas due to the strongly wavelength-dependent spectral characteristics of the underlying vegetation. They concluded that the CM SAF surface radiation CDR cannot be extended simply by applying the MagicSol algorithm to one of MSG's two narrowband visible channels (VIS006 and VIS008).

In this study, we evaluate the potential of a simulated broadband channel for a homogeneous extension of the CM SAF surface radiation CDR. This broadband channel is derived from the two narrowband visible channels (VIS006 and VIS008) following an approach of Cros, Albuisson, and Wald (2006) (see Section 3.1). The extended dataset covering the period 1983 to 2010 is validated against surface observations from the Baseline Surface Radiation Network (Ohmura et al., 1998) as well as intercompared to other surface radiation datasets (see Section 3.2). The retrieval of climatological time series from satellite data is often hampered by sensor degradation, spacecraft replacement and associated changes in spectral, temporal and spatial coverage and extent. Thus, in order to serve climate monitoring needs the extended surface radiation dataset have to be tested for homogeneity (see Section 3.3). The study concludes with an analysis of long-term trends and trend attribution (see Section 3.4).

2. Data and methods

2.1. Satellite data

The present study uses data from EUMETSAT's geostationary Meteosat satellites of the First and Second Generation. The satellites are located at a longitude of 0° (3.4°W for Meteosat 8) directly above the equator at an altitude of about 36,000 km. Both satellite generations have a field of view that extends to around 80°N/S and 80°E/W.

The CM SAF surface radiation CDR is generated with data from the MFG satellites. They carry the Meteosat Visible and Infrared Imager (MVIRI), a radiometer that measures the earth's disk every 30 min in 3 spectral bands covering visible and infrared wavelengths. The broadband visible channel (VISSN, 0.45–1 μm) employed in the derivation of the solar surface radiation has a spatial footprint (at nadir) of around 2.5 km.

The discussed extension is based on data from the MSG satellites carrying the Spinning Enhanced Visible and Infrared Imager (SEVIRI), a radiometer that measures the earth's disk every 15 min in 12 spectral bands spanning visible and infrared wavelengths. The two narrow band visible channels are centered at around 0.6 μm (VIS006) and 0.8 μm (VIS008) and have a spatial resolution of around 3 km at nadir. The SEVIRI broadband high-resolution-visible channel (HRV) closely matches the spectral properties of the MVIRI broadband channel. However, since it does not cover the full disk, it cannot be used to extend the full disk MVIRI-based CDR.

The overlap period between the two satellite generations in the years 2004 and 2005, when Meteosat 7 and 8 were measuring side by side, is used to calibrate the MagicSol algorithm to ensure a homogeneous continuation of the CM SAF surface radiation CDR with the MSG-based surface radiation dataset.

The input data from the SEVIRI and the MVIRI instruments are received from EUMETSAT's UMARF archive in Native or OpenMTP format, respectively. The output data (*SIS*, *SID* and *CAL*) is mapped onto a regular lon–lat grid with a 0.03° grid spacing using a triangulation method (CM SAF surface radiation CDR) or a nearest-neighbor technique (MSG-based surface radiation dataset).

2.2. MagicSol — Heliosat for climate data records

The CM SAF surface radiation CDR and the MSG-based extension presented here employ the MagicSol algorithm (Posselt et al., 2012). In summary, the solar surface irradiance is retrieved in a two-step approach. In the first step, the effective cloud albedo *CAL* (also known as cloud index) is retrieved using the Heliosat algorithm (Beyer et al., 1996; Cano et al., 1986; Hammer et al., 2003). The original Heliosat method was modified by including a self-calibration parameter ρ_{max} which represents the sensor's digital count corresponding to the brightest clouds seen by the satellite and an adapted algorithm to retrieve the clear-sky background field using 7-day running averages instead of fixed monthly values. In the second step, the clear sky irradiances are calculated using the look-up-table (LUT) based clear sky model "MAGIC" (Mueller et al., 2009). The surface radiation fluxes *SIS* and *SID* are subsequently obtained by combining the retrieved effective cloud albedo *CAL* with the clear sky irradiances.

2.3. Channel combination

An extension of the CM SAF surface radiation CDR based on either of SEVIRI's narrowband visible channels is not applicable due to the substantial spectral differences to the MVIRI broadband visible channel (VISSN) and the concurrent sensitivity of the resulting cloud albedo to the spectral differences of the land surface underlying the clouds (Posselt, Mueller, Stöckli, & Trentmann, 2011a). Hence, a simulated broadband visible channel for SEVIRI is used following an approach proposed by Cros et al. (2006). A simple linear combination model based on the radiances of SEVIRI's two narrowband visible channels (L_{VIS006} and L_{VIS008}) is applied to simulate the broadband radiance L_{broad} that corresponds to the radiance of the MVIRI VISSN channel (L_{VISSN}). The spectral channel characteristics of SEVIRI's narrowband channels and MVIRI's broadband channel are used to derive the combination parameters $\alpha_1 = 4.49459$ and $\alpha_2 = 2.36764$ so that

$$L_{broad} = \alpha_1 L_{VIS006} + \alpha_2 L_{VIS006}. \quad (1)$$

A subsequent regression with the MVIRI VISSN radiances implied the following small correction to the model to obtain a better agreement between L_{VISSN} and L_{broad}:

$$L_{broad,corr} = 1.0605\ L_{broad} + 0.5909. \quad (2)$$

The MagicSol algorithm requires digital counts *DC* as input which are obtained by inverting the standard calibration relation provided by EUMETSAT:

$$DC = ((L_\lambda)_{broad} - DC_0)/C. \quad (3)$$

The calibration coefficients $C = 0.028$ and the dark offset $DC_0 = -51\ C$ are chosen so that the resulting digital counts cover the range between 0 and 1023 which corresponds to the 10 bit encoding of the MSG data. The calibration relation 3 is given for the spectral radiance $(L_\lambda)_{broad}$ which is obtained from the radiance $L_{broad,corr}$ using the spectral properties of the MVIRI VISSN channel (maximum irradiance $I_{max} = 683.4\ W\ m^{-2}$) and the equivalent integrated solar irradiance $I_m = 69.8\ m\ W\ m^{-2}(cm^{-1})^{-1}$:

$$(L_\lambda)_{broad} = L_{broad,corr}(\pi I_m)/I_{max}. \quad (4)$$

The used radiances L_{VIS006}, L_{VIS008}, L_{VISSN}, L_{broad} and $L_{broad,corr}$ are given in [W m^{-2} s r^{-1}] whereas the spectral radiance $(L_\lambda)_{broad}$ is given in [W m^{-2} s r^{-1} μm^{-1}].

2.4. Validation and intercomparison data

Following the validation and intercomparison of the CM SAF surface radiation CDR shown in Posselt et al. (2012), the extended surface radiation dataset is validated using observations from the Baseline Surface Radiation Network (BSRN, Ohmura et al., 1998). Table 1 lists the BSRN stations used in the validation. At every BSRN station the maximum available overlap period is used for the validation of the satellite data. Thereby, stations with a maximum overlap of less than 12 months are

Table 1
BSRN stations used for the validation (and their respective position on the Meteosat disk).

Station	Country	Code	Data since
Bermuda	Bermuda	ber	01/1992
Brasilia	Brazil	brb	02/2006
Cabauw	Netherlands	cab	12/2005
Camborne	UK	cam	01/2001
Carpentras	France	car	08/1996
De Aar	South Africa	daa	05/2000
Florianopolis	Brazil	flo	06/1994
Lerwick	UK	ler	01/2001
Lindenberg	Germany	lin	09/1994
Palaiseau	France	pal	05/2003
Payerne	Switzerland	pay	09/1992
Sede Boger	Israel	sbo	01/2003
Solar Village	Saudi Arabia	sov	08/1998
Tamanrasset	Algeria	tam	03/2000
Toravere	Estonia	tor	01/1999

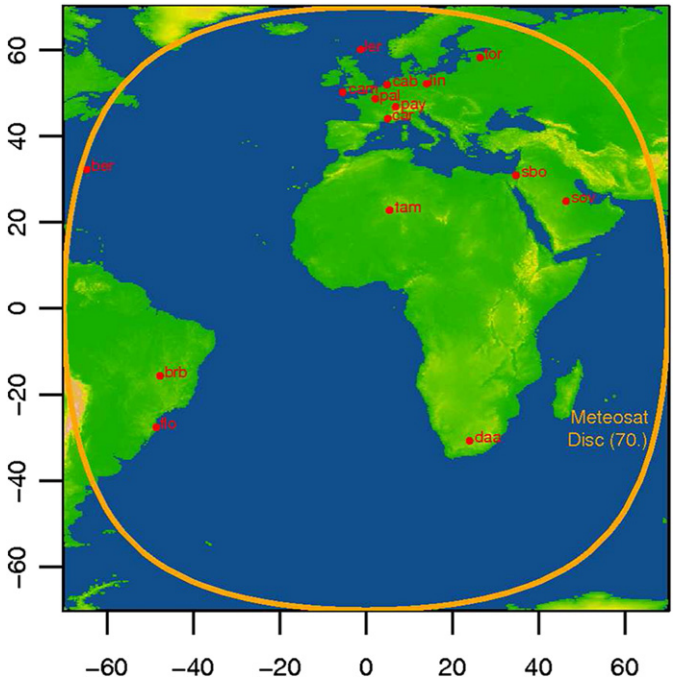

discarded. Unfortunately, most of the available 15 stations are found in the northern hemisphere. However, the main climatic regions are covered.

The validation of the monthly and daily means was carried out. As the results follow mainly the same reasoning presented in Posselt et al. (2012) (as will be shown in Section 3.2), the validation part of the current study is confined to the monthly means only. The applied validation threshold for the monthly mean *SIS* is 15 W m^{-2}, the target and the optimal accuracy are 10 W m^{-2} and 8 W m^{-2}, respectively, using the mean absolute bias (MAB) as accuracy measure. Furthermore, Ohmura et al. (1998) state a non-systematic error of 5 W m^{-2} for BSRN's solar irradiance measurements which is considered in the validation.

Intercomparison datasets are used to evaluate the quality of the extended surface radiation dataset. These datasets include the "HC1" dataset from the HelioClim-Project (Cros, Albuisson, Lefevre, Rigollier, & Wald, 2004; Lefèvre, Wald, & Diabaté, 2007), the ISCCP FD (Rossow & Dueñas, 2004) and the GEWEX SRB (Gupta, Stackhouse, Cox, Mikovitz, & Zhang, 2006) as well as the ECMWF's model-based re-analysis dataset ERA-Interim (Dee et al., 2011). The same time period is used for the intercomparison and evaluation of all monthly mean datasets. Further details on the intercomparison datasets are given in Posselt et al. (2012).

2.5. Homogeneity test

The homogeneity of the CM SAF surface radiation CDR was investigated by Brinckmann and Ahrens (2012) and Schibli (2011). Among others, they used the Standard Normal Homogeneity Test (SNHT, Alexandersson, 1986) to assess the homogeneity to the full MFG-based dataset from 1983 to 2005. The SNHT will also be used in this study to show the applicability of the above described channel combination in generating a homogeneous extension to the CM SAF surface radiation CDR.

The SNHT searches for discontinuities in a time series which might include breaks or shifts but also short- and long-term trends. Adapted from Alexandersson (1986), the test value $T(k)$ is calculated for each time step k of the considered time series.

$$T(k) = k\bar{z}_1^2 + (n-k)\bar{z}_2^2 \quad \text{with } k = 1,\ldots,n. \tag{5}$$

The standardized means $\bar{z}_1$ and $\bar{z}_2$ are calculated using the mean $\overline{Y}$ and the standard deviation s of the whole considered time series.

$$\bar{z}_1 = \frac{1}{k}\sum_{i=1}^{k}\frac{(Y_i-\overline{Y})}{s}$$
$$\bar{z}_2 = \frac{1}{n-k}\sum_{i=k+1}^{n}\frac{(Y_i-\overline{Y})}{s}. \tag{6}$$

Large differences between $\bar{z}_1$ and $\bar{z}_2$ point to different mean values and, thus, a shift at time step k which is reflected in high values for $T(k)$. If $T(k)$ exceeds a certain critical (confidence) level T_c a break point is detected at $T_0 = max(T(k))$. The values of T_c depend on the length of the time series and the chosen confidence level. In this study, T_c values provided by Khaliq and Ouarda (2007) for the 95%-confidence level are used.

Similar to Brinckmann and Ahrens (2012), the "relative homogeneity testing" (test series minus reference series) is applied using radiation data from ERA-Interim as reference. It enables a comprehensive spatial and temporal evaluation of the homogeneity of the extended surface radiation dataset that cannot be achieved using a few surface sites over a limited time period. However, an "absolute homogeneity testing" of the ERA-Interim data by Brinckmann and Ahrens (2012) revealed some considerable inhomogeneities especially in the tropics. Thus, the homogeneity analysis excludes the equatorial band between 12° South and North to prevent attributing those inconsistencies to the satellite-derived surface radiation dataset.

The homogeneity analysis is conducted regionally using spatial means of the extended surface radiation dataset and ERA-Interim. Further, monthly anomalies (representing the deviation of the monthly mean from the long-term monthly mean) are used for all time series to eliminate annual and seasonal variability. Inhomogeneities found in the first and the last 10 months of the time series are discarded as the SNHT is not reliable to detect significant breaks at the beginning and at the end of the time series (Toreti et al., 2011).

3. Results

3.1. Channel combination

The overlap period between Meteosat 7 and 8 in the years 2004 and 2005 is used to evaluate the agreement between the MVIRI and the SEVIRI based solar surface radiation time series. Fig. 1 shows the monthly means of *CAL* spatially averaged over the Meteosat disk for the MVIRI (black line) and the SEVIRI based surface radiation data using the simulated broadband channel (blue line). It can be seen that there is a very good agreement in the annual cycle between those two time series but with a systematic offset (bias) of 0.0142.

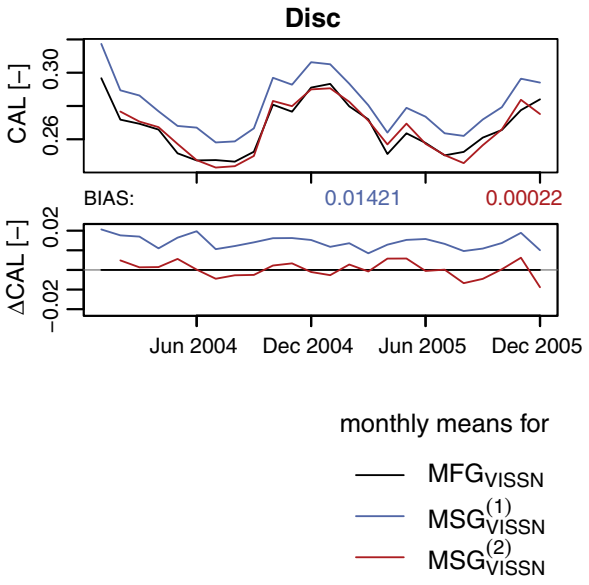

Fig. 1. Monthly Mean *CAL* during overlap period for the CM SAF Surface Radiation CDR (black line) and the MSG-based Surface Radiation Dataset (blue line: channel combination only, red line: channel combination and adapted ρ_{max}).

This bias is due to differences in the range of the input data (i.e., brightest vs. darkest pixel) which is in the order of 25–30 digital counts *DC* higher for Meteosat 8 than for Meteosat 7 (using the respective differences between the 95% and 5% percentile of all DCs on the Meteosat disk and applying the 10 bit encoding of the MSG data for Meteosat 7 as well). The Heliosat algorithm is sensitive to the dynamic range of the digital counts *DC* since it contains threshold tests (e.g., for snow detection) which depend on the calibration parameter ρ_{max} (corresponds to the brightest pixels). Thus, in order to minimize this full-disk-bias of *CAL*, ρ_{max} has to be adapted. The processing of the CM SAF surface radiation CDR used a correction factor for ρ_{max} of 1.05. For the SEVIRI-based surface radiation dataset this factor was increased to 1.105 which reduced the bias to −0.00022 (Fig. 1, red line).

Fig. 2 shows the spatial distribution of the absolute differences of the seasonal means of *CAL* for December–January–February (DJF, upper row) and June–July–August (JJA, lower row) between *CAL* derived from MVIRI and from the two SEVIRI channels (left column for VIS006, middle column for VIS008) and the simulated SEVIRI broadband channel (right column). Bias and MAB for the full disk are given below the respective plots.

The simulated broadband VISSN channel and the adaptation of ρ_{max} leads to a decrease in bias and MAB for both seasons compared to the narrowband VIS channels of SEVIRI. The differences between MVIRI and SEVIRI derived *CAL* are small for the simulated VISSN channel. Especially over Africa the influence of the spectral differences of the VIS channels is reduced by simulating the broadband channel. The large differences at the northern and southern rim of the disk, which were attributed to differences in the value range between MVIRI and SEVIRI in Posselt, Mueller, Stöckli, and Trentmann (2011a), also disappear. However, another issue becomes evident when comparing MVIRI and SEVIRI *CAL* — a gradually shift from underestimation MVIRI *CAL* values in the East to overestimating MVIRI *CAL* values in the West. This is most likely due to the different positions of the Meteosat 7 (0°) and Meteosat 8 (3.4°W). Although the geolocation is corrected by EUMETSAT the satellite viewing geometry of Meteosat 8 remains different from Meteosat 7.

3.2. Validation and intercomparison

The quality of the extended surface radiation dataset is evaluated using different statistical parameters. Those include the commonly used bias and the MAB as well as the standard deviation (SD). Further, the correlation of the anomalies (AC) and the fraction of months that exceed the accuracy threshold ($Frac_{mon}$) are provided. The definition of the applied quality measures is given in Appendix A.

The validation results for the monthly mean *SIS* of the extended surface radiation dataset at all BSRN stations are summarized in Table 2. The number of available BSRN observations nearly doubled (from 855 in Posselt et al. (2012) to 1543) due to the longer, extended satellite time series and additional BSRN stations.

The extended dataset shows a MAB that is well below the required accuracy threshold (15 W m^{-2}) and it is only slightly higher than the optimal accuracy threshold (8 W m^{-2}). The target accuracy is only exceeded in 13.55% of all monthly means. The high anomaly correlation

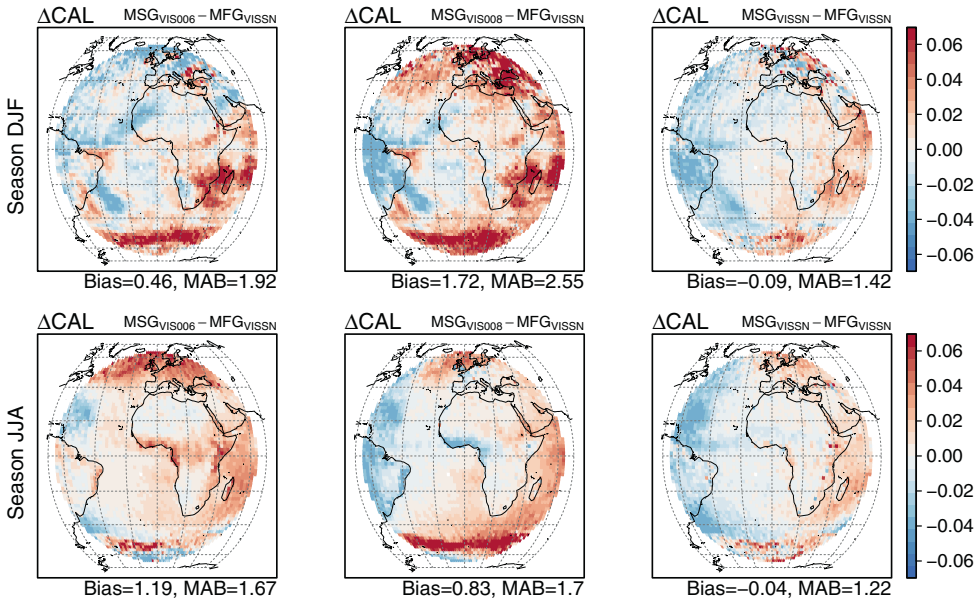

Fig. 2. Seasonal differences (DJF: top row, JJA: bottom row) between Meteosat 8 (MSG) visible channels (VIS006: left column, VIS008: middle column, simulated VISSN: right column) and Meteosat 7 (MFG).

Table 2
Statistics for the comparison of monthly mean *SIS* between BSRN and the extended surface radiation dataset (CM SAF), HelioClim HC1, ERA-Interim, GEWEX SRB and ISCCP FD.

SIS (Monthly mean)	n_{mon}	Bias [W m^{-2}]	MAB [W m^{-2}]	SD [W m^{-2}]	AC	$Frac_{mon}$ [%]
CM SAF	1543	3.16	8.15	10.47	0.90	13.55
HelioClim	903	−15.09	21.34	18.55	0.78	55.59
ERA-Interim	1543	4.09	9.12	12.92	0.89	17.95
GEWEX SRB	1241	−2.85	11.34	12.77	0.86	29.09
ISCCP FD	1469	−2.3	10.39	12.38	0.88	24.37

of 0.9 reveals that the extended surface radiation dataset is able to capture the monthly mean anomalies of *SIS* measured at the surface. Table 2 also includes the corresponding values of the intercomparison datasets. The results are similar to those presented in Posselt et al. (2012). The extended surface radiation dataset shows the highest quality compared to the evaluated datasets for nearly all quality quantities. The intercomparison datasets show a considerably larger spread (SD) and $Frac_{mon}$ which results in higher uncertainties. The better performance of the extended surface radiation dataset might be partly caused by the higher spatial resolution and, thus, an improved co-location with the BSRN stations.

The absolute bias by BSRN station is shown in Fig. 3. The extended surface radiation dataset shows the lowest MAB of all five monthly mean datasets and a consistently low spread. As already found in Posselt et al. (2012), for some stations the HelioClim HC1 dataset exhibits extremely large deviations from the surface measurements and from the other intercomparison datasets. In comparison to the extended surface radiation dataset and ERA-Interim, ISCCP FD and GEWEX SRB strongly underestimate *SIS* at the desert stations of Sede Boqer (sbo), Solar Village (svo) and Tamanrasset (tam). The performance of the extended surface radiation dataset improved at the station Lerwick (ler) compared to the MFG-only CM SAF surface radiation CDR.

3.3. Homogeneity

The tests assessing the homogeneity of the CM SAF surface radiation dataset and the presented extension using SEVIRI data are carried out for the period 1994 to 2010. The 1980s are discarded due to the apparent discontinuity during the operation phases of Meteosat 3 (1988–1989, 3 months in 1990 as replacement for Meteosat 4, backup for Meteosat 4 until 1994) which was found by Brinckmann and Ahrens (2012) and is illustrated in Fig. 4. In the upper panel the full time series starting in 1983 for the extended surface radiation dataset and ERA-Interim are shown. The difference between the two time series and the respective detrended time series are shown in the middle panel. The lower panel shows the SNHT test value *T* for the difference and the detrended difference time series. The vertical dashed lines illustrate

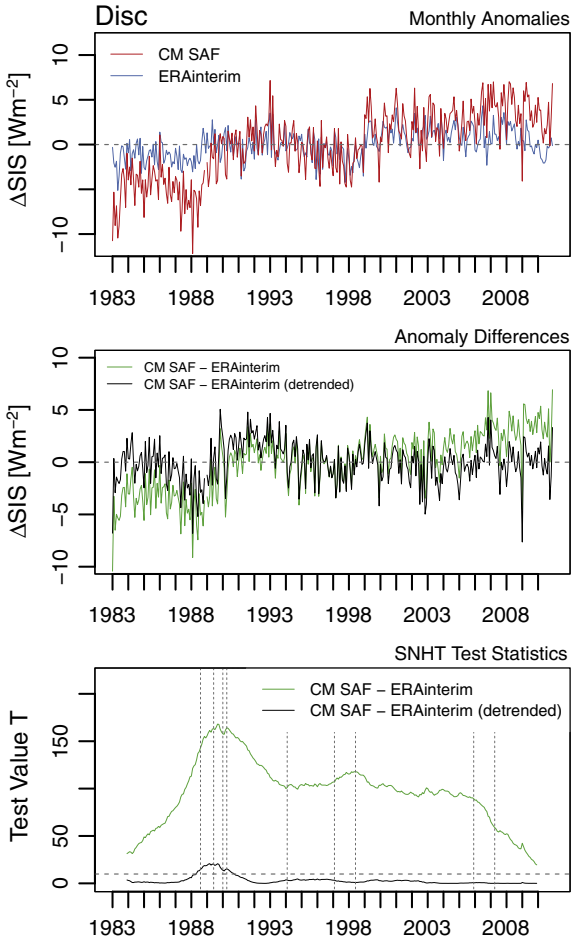

Fig. 4. Full disk means of the extended surface radiation dataset (CM SAF) and ERA-Interim *SIS* (1983–2010) and the corresponding SNHT test statistics for the difference and detrended difference series. Note that the equatorial region between 12° South and North is excluded from the Disk.

the satellite changes. Simply calculating the SNHT from the difference of the two time series results in a very broad distribution of *T*. This points to a long-term trend in the differences between the extended surface radiation dataset and ERA-Interim (Brinckmann and Ahrens 2012). Using the difference of the detrended time series yields a clear detection of a break around 1989–1990. During this time period several satellite changes took place. Thus, the remaining analysis is restricted to the time period after 1994 when Meteosat 3 was finally decommissioned. This is justified since the aim of this study is to evaluate the homogeneity of the extension after 2004.

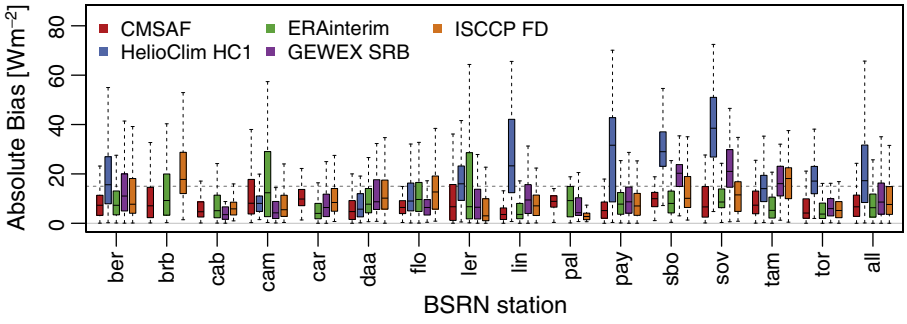

Fig. 3. Absolute bias [W m^{-2}] of *SIS* for the monthly difference between BSRN surface measurements and the extended surface radiation dataset (CM SAF), HelioClim, ERA-Interim, GEWEX SRB and ISCCP FD, respectively.

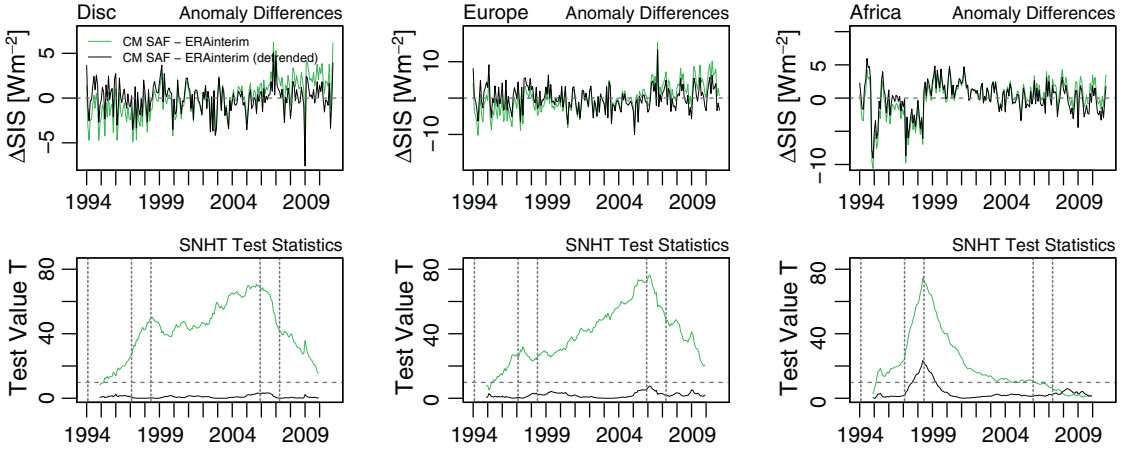

Fig. 5. Anomaly difference between the extended surface radiation dataset (CM SAF) and ERA-Interim *SIS* (1994–2010) and the corresponding SNHT test statistics for the difference and detrended difference series for different regions. Note that the equatorial region between 12° South and North is excluded from the Disk and Africa, respectively.

Fig. 5 and Table 3 show the results of the SNHT test of the reduced time series for various regions. Fig. 5 shows that the distribution of T is very broad for the difference time series (for the full disk (left column) and Europe (middle column)) resulting from the long-term trend in the differences between the extended surface radiation dataset and ERA-Interim. In Africa (right column) the trend is much smaller and, thus, has less influence on the shape of the Test Value T. Using the detrended difference time series no significant breaks are detected for most of the regions except Africa. However, Fig. 5 displays a local maximum during 2005–2006 in all three presented regions but the critical level T_c is not exceeded. In Africa, a break is detected at the change from Meteosat 6 to Meteosat 7 in May 1998 which was also detected and discussed by Brinckmann and Ahrens (2012) (see their Fig. 11D).

3.4. Trend analysis and attribution

Section 3.3 showed that, except for Africa, the extended surface radiation dataset from 1994 to 2010 is homogeneous and can be used for trend analysis. For the trend analysis a standard statistical linear regression model with slope (which corresponds to the trend) and intercept as parameters is used (Wilks, 2006). Table 3 lists the trends (together with the corresponding significance levels) of *SIS* for the Meteosat-based surface radiation dataset and ERA-Interim. The analysis left out Africa due to the detected break in 1998. Further, the equatorial region is excluded from the considered regions because the homogeneity could not be tested. The other intercomparison datasets are also taken out of the trend analysis because they are not yet tested for homogeneity. Further, comparison with trends of BSRN station data provided hints for artifacts in the trends of ISCCP FD and GEWEX SRB from 1993 onwards (Mueller, Trentmann, Träger-Chatterjee, Posselt, & Stöckli, 2011).

Table 3
Regional trends (1994–2010) [W m^{-2} dec^{-1}] for *SIS*, $SIS_{CAL,clim}$ and $SIS_{CS,clim}$ of the extended surface radiation dataset as well as for ERA-Interim.
Note that the equatorial region between 12° South and North is excluded from the considered regions (disk, land, ocean).

Region	*SIS*	$SIS_{CAL,clim}$	$SIS_{CS,clim}$	ERA-Interim
Disk	3.43***	−0.16	3.59***	0.86***
Land	3.63***	0.01	3.63***	0.55*
Europe	4.35**	−0.3***	4.65**	0.7
Ocean	3.34***	−0.23*	3.57***	1***
North Atlantic	6.15***	−0.22**	6.37***	0.99**
South Atlantic	3.63***	−0.18	3.79***	1.25***

Significance levels: 0, '***' 0.001, '**' 0.01, '*' 0.05, '.' 0.1.

All considered regions show positive trends for the extended CM SAF surface radiation dataset pointing to an increase in solar surface radiation and, thus, a brightening by either a decrease in cloudiness or a decreased atmospheric absorption of solar radiation. However, the extent and also the significance of the trends in the different regions vary substantially. The trend for Europe of 4.35 W m^{-2} dec^{-1} is in the order of trends derived from surface measurements by Wild (2012) of 2 W m^{-2} dec^{-1} for the 1980s to 2000 and 3 W m^{-2} dec^{-1} after 2000. Table 3 also shows that the trends derived from ERA-Interim point mostly in the same direction but are much less pronounced and less significant.

In order to estimate the contribution of SIS_{CS} (i.e., representing changes in the atmospheric absorption) and *CAL* (i.e., representing the changes in cloudiness) to the trend, two "pseudo" *SIS* time series are generated. The climatological daily mean annual cycle of SIS_{CS} ($=SIS_{CS,clim}$) and *CAL* ($=CAL_{clim}$) is used together with the time series of *CAL* and SIS_{CS}, respectively, to form the "pseudo" *SIS* time series:

$$SIS_{CALclim} = k(CAL_{clim})SIS_{cs} \quad \Rightarrow \text{Trend contribution from } SIS_{cs} \tag{7}$$

$$SIS_{CSclim} = k(CAL)SIS_{cs,clim} \quad \Rightarrow \text{Trend contribution from } CAL. \tag{8}$$

The relation between k (clear sky index) and *CAL* is given in Posselt et al. (2012) (Eq. (3)) and over a wide range of *CAL*, it is $k(CAL) = 1 - CAL$.

Table 3 lists the regional trends for *SIS*, $SIS_{CAL,clim}$ and $SIS_{CS,clim}$. The trends of *SIS* and $SIS_{CS,clim}$ are very similar for all regions. Thus, within the extended Meteosat-based surface radiation dataset the trends in global radiation are mainly due to changes in the cloudiness. The trends in $SIS_{CAL,clim}$ are an order of magnitude smaller than the trends in *SIS* or $SIS_{CS,clim}$ and are attributed only to trends in the water vapor fields. The direct aerosol effects, that would be also visible as trends in $SIS_{CAL,clim}$, are not considered because only climatological aerosol fields are used in the calculation of SIS_{CS}. Thus, concerning aerosols only indirect effects on the clouds might contribute to the trends of *CAL* and, subsequently, to the trends of *SIS*.

4. Summary and conclusion

In order to serve climate monitoring needs the CM SAF surface radiation CDR has to be continuously extended into the present. Posselt, Mueller, Stöckli, and Trentmann (2011a) demonstrated that no simple

continuation of this CDR is possible from Meteosat First Generation to Meteosat Second Generation due to the spectral sensitivity of effective cloud albedo to the underlying surface. A linear combination of the two narrow-band visible channels of MSG's SEVIRI instrument to a simulated broadband channel similar to the MVIRI VISSN channel was therefore applied in this study. The overlap period in 2004 and 2005 was used to adapt the single self-calibration parameter ρ_{max} to the simulated broadband channel. The results of the homogeneity analysis show that the SEVIRI surface radiation dataset can be used to extend the CM SAF surface radiation CDR into the present. The extended dataset complies with GCOS-defined validation thresholds.

Unfortunately, the 28-year long dataset is found not to be suitable for climatological analysis due to a large inhomogeneity in the late 1980s. However, a reduced dataset starting in 1994 is sufficiently homogeneous in most of the investigated regions (except of Africa) to be used for spatially distributed climatological analysis. Trend analysis (starting in 1994) indicate that the trend on the Meteosat disk is positive for *SIS* but with varying extents for the different regions. This could be due to changes in cloudiness or due to changes in the clear sky state of the atmosphere. We demonstrate that most of the trends in the surface radiation dataset is caused by changes in the cloudiness (i.e., *CAL*) which can be due to changes in either circulation patterns or indirect aerosol effects. No statement can be made about the magnitude of the direct aerosol effect (which would result in trends in the clear sky radiation) since an aerosol climatology is used as boundary conditions for the clear sky model.

Acknowledgments

The study was carried out as part of EUMETSAT's Satellite Application Facility on Climate Monitoring (CM SAF) also using datasets provided by CM SAF. The contribution of data from all the various field sited to the BSRN archive and its maintenance at the AWI is greatly appreciated. The Swiss National Supercomputing Centre (CSCS) is acknowledged for providing computing and archiving resources and user support for this project. We want to thank M. Wild (and colleagues) for an ongoing conversation and discussion about climate analysis of radiation data.

Appendix A. Statistical measures for the validation

In the following, the applied quality measures are described. The definitions of the statistical measures are taken from Wilks (2006). Thereby, the variable y describes the dataset to be validated (e.g., CM SAF) and o denotes the reference dataset (i.e., BSRN). The individual time step is marked with k and n is the total number of time steps.

Bias

The bias (or mean error) is the mean difference between the two considered datasets and indicates an average over- or underestimating regarding the reference dataset.

$$\text{Bias} = \frac{1}{n}\sum_{k=1}^{n}(y_k - o_k) = \overline{y} - \overline{o}. \tag{A.1}$$

Mean absolute bias (MAB)

The mean absolute bias (MAB) is the average of the absolute differences between the time series.

$$\text{MAB} = \frac{1}{n}\sum_{k=1}^{n}|y_k - o_k|. \tag{A.2}$$

Standard deviation (SD)

The standard deviation SD is a measure for the spread around the mean value of the distribution formed by the differences between the time series.

$$\text{SD} = \sqrt{\frac{1}{n-1}\sum_{k=1}^{n}((y_k - o_k) - (\overline{y} - \overline{o}))^2}. \tag{A.3}$$

Anomaly correlation (AC)

The anomaly correlation AC describes to which extend the anomalies of the two considered time series correspond to each other without the influence of a possibly existing bias.

$$\text{AC} = \frac{\sum_{k=1}^{n}(y_k - \overline{y})(o_k - \overline{o})}{\sqrt{\sum_{k=1}^{n}(y_k - \overline{y})^2}\sqrt{\sum_{k=1}^{n}(o_k - \overline{o})^2}}. \tag{A.4}$$

Here, for each station the mean annual cycle is derived separately from the satellite and surface data, respectively. The monthly anomalies are calculated using the corresponding mean annual cycle as the reference.

Fraction of time steps above the validation threshold (Frac)

A measure for the uncertainty of the derived dataset is the fraction of the time steps that are outside the requested thresholds *Th*.

$$\text{Frac} = 100\frac{\sum_{k=1}^{n} f_k}{n} \quad \text{with} \quad \begin{cases} f_k = 1 & \text{if } y_k > \text{Th} \\ f_k = 0 & \text{otherwise} \end{cases}. \tag{A.5}$$

References

Alexandersson, H. (1986). A homogeneity test applied to precipitation data. *Journal of Climatology*, *6*, 661–675. http://dx.doi.org/10.1002/joc.3370060607 (URL: http://dx.doi.org/10.1002/joc.3370060607)

Beyer, H. G., Costanzo, C., & Heinemann, D. (1996). Modifications of the Heliosat procedure for irradiance estimates from satellite images. *Solar Energy*, *56*, 207–212.

Brinckmann, S., & Ahrens, B. (2012). Evaluation and assessment of the CM-SAF surface solar radiation climate data records. *Visiting scientist report. EUMETSAT Satellite Application Facility on Climate Monitoring* (URL: http://www.cmsaf.eu. (derived publication submitted))

Cano, D., Monget, J. M., Albuisson, M., Guillard, H., Regas, N., & Wald, L. (1986). A method for the determination of the global solar-radiation from meteorological satellite data. *Solar Energy*, *37*, 31–39.

Cros, S., Albuisson, M., Lefevre, M., Rigollier, C., & Wald, L. (2004). HelioClim: A long-term database on solar radiation for Europe and Africa. *Proceedings of Eurosun 2004*, *3*. (pp. 916–920)Freiburg, Germany: PSE GmbH.

Cros, S., Albuisson, M., & Wald, L. (2006). Simulating Meteosat-7 broadband radiances using two visible channels of Meteosat-8. *Solar Energy*, *80*, 361–367.

Dee, D. P., Uppala, S. M., Simmons, A. J., Berrisford, P., Poli, P., Kobayashi, S., et al. (2011). The ERA-Interim reanalysis: Configuration and performance of the data assimilation system. *Quarterly Journal of the Royal Meteorological Society*, *137*, 553–597. http://dx.doi.org/10.1002/qj.828 URL: http://dx.doi.org/10.1002/qj.828

GCOS (2006). Systematic observation requirements for satellite-based products for climate — Supplemental details to the GCOS implementation plan. *Technical Report. GCOS-107 (WMO-TD/No. 1338)*.

GCOS (2010). Implementation plan for the global observing system for climate in support of the UNFCCC (2010 Update). *Technical Report. GCOS-138 (WMO-TD/No. 1523)*.

Gupta, S., Stackhouse, P., Jr., Cox, S., Mikovitz, J., & Zhang, T. (2006). Surface radiation budget project completes 22-year data set. *GEWEX News*, *16*, 12–13.

Hammer, A., Heinemann, D., Hoyer, C., Kuhlemann, R., Lorenz, E., Müller, R., et al. (2003). Solar energy assessment using remote sensing technologies. *Remote Sensing of Environment*, *86*, 423–432.

Khaliq, M. N., & Ouarda, T. B.M. J. (2007). On the critical values of the standard normal homogeneity test (SNHT). *International Journal of Climatology*, *27*, 681–687. http://dx.doi.org/10.1002/joc.1438 URL: http://dx.doi.org/10.1002/joc.1438

Lefèvre, M., Wald, L., & Diabaté, L. (2007). Using reduced data sets ISCCP-B2 from the Meteosat satellites to assess surface solar irradiance. *Solar Energy*, *81*, 240–253.

Mueller, R., Matsoukas, C., Gratzki, A., Behr, H., & Hollmann, R. (2009). The CM-SAF operational scheme for the satellite based retrieval of solar surface irradiance — A LUT based eigenvector hybrid approach. *Remote Sensing of Environment*, *113*, 1012–1024. http://dx.doi.org/10.1016/j.rse.2009.01.012.

Mueller, R., Trentmann, J., Träger-Chatterjee, C., Posselt, R., & Stöckli, R. (2011). The role of the effective cloud albedo for climate monitoring and analysis. *Remote Sensing*, *3*, 2305–2320. http://dx.doi.org/10.3390/rs3112305 URL: http://www.mdpi.com/2072-4292/3/11/2305,

Ohmura, A., Dutton, E. G., Forgan, B., Fröhlich, C., Gilgen, H., Hegner, H., et al. (1998). Baseline surface radiation network (BSRN/WCRP): New precision radiometry for climate research. *Bulletin of the American Meteorological Society*, *79*, 2115–2136.

Posselt, R., Mueller, R., Stöckli, R., & Trentmann, J. (2011). Spatial and temporal homogeneity of solar surface irradiance across satellite generations. *Remote Sensing*, *3*, 1029–1046. http://dx.doi.org/10.3390/rs3051029.

Posselt, R., Mueller, R., Stöckli, R., & Trentmann, J. (2012). Remote sensing of solar surface radiation for climate monitoring — The CM-SAF retrieval in international comparison. *Remote Sensing of Environment*, *118*, 186–198. http://dx.doi.org/10.1016/j.rse.2011.11.01 (URL: http://www.sciencedirect.com/science/article/pii/S0034425711004111)

Posselt, R., Mueller, R., Stockli, R., & Trentmann, J. (2011). CM SAF surface radiation MVIRI data set 1.0 (URL: http://dx.doi.org/10.5676/EUM_SAF_CM/RAD_MVIRI/V001, http://dx.doi.org/10.5676/EUM_SAF_CM/RAD_MVIRI/V001)

Rossow, W. B., & Dueñas, E. N. (2004). The International Satellite Cloud Climatology Project (ISCCP) web site: An online resource for research. *Bulletin of the American Meteorological Society*, *85*, 167–172. http://dx.doi.org/10.1175/BAMS-85-2-167.

Schibli, R. (2011). Spatio-temporal homogeneity of a satellite-derived global radiation climatology. *Veröffentlichungen der MeteoSchweiz*, *88*, 110.

Schulz, J., Albert, P., Behr, H., Caprion, D., Deneke, H., Dewitte, S., et al. (2009). Operational climate monitoring from space: The EUMETSAT satellite application facility on climate monitoring (CM-SAF). *Atmospheric Chemistry and Physics*, *9*, 1687–1709.

Climate change 2007: The physical science basis. Solomon, S., Qin, D., Manning, M., Chen, Z., Marquis, M., & Averyt, K., et al. (Eds.). (2007). *Contribution of working group I to the fourth assessment report of the Intergovernmental Panel on Climate Change*. Cambridge, United Kingdom and New York, NY, USA: Cambridge University Press.

Toreti, A., Kuglitsch, F. G., Xoplaki, E., Della-Marta, P.M., Aguilar, E., Prohom, M., et al. (2011). A note on the use of the standard normal homogeneity test to detect inhomogeneities in climatic time series. *International Journal of Climatology*, *31*, 630–632. http://dx.doi.org/10.1002/joc.2088 (URL: http://dx.doi.org/10.1002/joc.2088)

Wild, M. (2012). Enlightening global dimming and brightening. *Bulletin of the American Meteorological Society*, *93*, 27–37. http://dx.doi.org/10.1175/BAMS-D-11-00074.1.

Wilks, D. S. (2006). Statistical methods in the atmospheric sciences (2nd ed.)*International Geophysics Series*. Academic Press.